Computer Assisted Methods in Engineering and Science
31(1): 29–50, 2024, doi: 10.24423/cames.1008

Modeling of Photochemical and Photothermal Effects in Soft Tissue Subjected to Laser Irradiation

Marek JASIŃSKI*, Maria ZADOŃ

Department of Computational Mechanics and Engineering, Silesian University of Technology, Gliwice, Poland; e-mail: maria.zadon@polsl.pl

* *Corresponding Author e-mail: marek.jasinski@polsl.pl*

The purpose of this study is to analyze the phenomena that occur in biological tissue during photodynamic therapy (PDT). Under the influence of the laser, triplet oxygen is transformed into singlet oxygen, which is cytotoxic to cancer tissue. The impact of the laser on the tissue may also be accompanied by changes in the thermophysical parameters, e.g., perfusion, which can affect the supply of oxygen to the tissue and, consequently, the outcome of the therapy. The proposed model uses the optical diffusion equation, the Pennes bioheat transfer equation, and reactions equations for PDT. The connection between bioheat transfer and PDT models is taken into account through the respective relationships between perfusion rate, capillary blood velocity, and the maximum oxygen supply rate. Furthermore, a method is proposed to model abnormal vascular patterns in the tumor subdomain. The boundary element method and the finite difference method were used in the numerical implementation stage.

Keywords: bioheat transfer, optical diffusion equation, photodynamic therapy, boundary element method, finite difference method.

1. Introduction

Numerous effects occur in biological tissue during laser irradiation. They may be related to various photochemical reactions or changes resulting from a local increase in tissue temperature. In some situations, alterations occur due to photoablation or photodisruption. These effects find applications in various medical procedures. An example of a treatment that uses photochemical and sometimes photothermal effects is photodynamic therapy (PDT) aimed at destroying cancer cells [1–3].

The photochemical effects that occur during PDT therapy are mainly linked to the transition of the basic form of oxygen in the body, from the triplet

form ($^3O_2$) to the singlet form of oxygen ($^1O_2$). The latter form is highly cytotoxic to cancer cells. The transition of triplet oxygen to singlet oxygen requires the presence in the tissue of a special substance called a photosensitizer (S_0). In Type I reactions, direct interaction of the excited photosensitizer is used. In Type II reactions, the photosensitizer interacts with triplet oxygen, which is then transferred to an excited singlet state [4–7].

As already mentioned, a laser's impact on tissue can result in an elevation of its temperature. Usually, an increase of the temperature in the tissue during PDT treatment does not lead to thermal damage to the tissue (except for variations of PDT that use temperature as an additional therapeutic effect) [1, 2]. However, it is known that even a small increase in tissue temperature can cause a change in tissue parameters. A good example is the perfusion coefficient, sometimes considered an indicator of tissue thermal damage. With small increases in temperature, perfusion increases. However, as the temperature rises further, thermal damage to the tissue increases, causing the destruction of blood vessels and the subsequent disappearance of perfusion. Since blood is an oxygen carrier, changes in perfusion can affect oxygen concentration when performing a PDT procedure [8–10].

Cancer tissue is distinctly different from healthy tissue. Differences are related, among other things, to an abnormal vascular pattern in tumor tissue, microthrombosis, and hypoxia. An abnormal vascular pattern means that the capillaries, the smallest blood vessels in tissue, responsible for the delivery of oxygen to the tissue, are irregularly distributed in tumor tissue, often assuming irregular shapes. They could be in form, e.g. bulbs instead of the typical pipes. They often exhibit a chaotic and tortuous configuration, with some capillaries being blind-ended. This kind of pattern often leads to microthrombosis, which results in hypoxia – oxygen deficiency in the tumor tissue. Therefore, when considering the potential effects of cancer therapies, it is important to take into account irregularities in the tumor subdomain and the unevenly occurring phenomena [5, 7, 11, 12].

In the current work, we present a model that takes into account both the photochemical reactions occurring during PDT treatment and the accompanying photothermal phenomena induced by laser irradiation to the tissue. The impact of parameters on perfusion values is also considered, as well as the effect of variable perfusion on oxygen delivery to the tissue. In addition, we propose a tumor tissue model that incorporates irregularities in the tumor tissue area, stemming from an abnormal vascular pattern. So far, models related to bioheat transfer and reactions during PDT have been considered separately, making the presented model a novel contribution to the field.

To describe light propagation in biological tissues, different mathematical models can be used. Some of them are based on the radiative transport equation.

To solve such an equation, several modifications of the discrete ordinates method and statistical Monte Carlo methods are commonly used. In this paper, the optical diffusion equation is employed. This is because the scattering generally dominates over the absorption in soft tissues for wavelengths between 650 and 1300 nm [13–18].

There are different equations for modeling bioheat transfer. The oldest and still the most commonly used model to determine temperature distribution in biological tissue is the Pennes equation founded on the classical Fourier law of heat conduction [8, 10, 19–25]. The other models of bioheat transfer, such as the hyperbolic Cattaneo–Vernotte equation or the dual-phase lag model, take into account the heterogeneous structure of biological tissue [16, 22, 26–34]. In the current paper, the Pennes equation is used.

As already mentioned, temperature increases during PDT treatment generally do not lead to thermal tissue damage. However, there is a set of formulas that precisely link the values of the thermophysical (perfusion coefficient) or optical (scattering coefficient) tissue parameters with thermal tissue damage. For this reason, we also use the Arrhenius scheme in this work, which is one of the ways for modeling thermal damage to biological tissue [9, 10, 20, 26, 35].

During PDT therapy, oxygen transits from the ground state (tripled oxygen $^3O_2$) to the excited state (singlet oxygen $^1O_2$), which is accompanied by phenomena such as absorption, fluorescence, energy transfer, and photobleaching. All these phenomena are included in the model that describes the photochemical reactions occurring during PDT. The complete set of equations is usually used in a simplified form to account for the concentration of the three main components: triplet oxygen, singlet oxygen, and a photosensitizer [4–7].

The models for bioheat transfer and reactions during PDT treatment are linked by relationships that consider changes in perfusion and the resulting change in capillary blood velocity, which, in turn, affect the oxygen maximum supply rate – an important parameter in the PDT model. This parameter is generally determined based on the so-called Krogh cylinder model, which, in many cases, requires rather large computational effort. For this reason, the current work uses a simplified formula to determine the time-dependent value of this parameter [5, 36–39].

Essentially, the goal of this work is to analyze the relationship between bioheat transfer, perfusion, oxygen supply to the tissue, and oxygen use in PDT treatment. In the context of bioheat transfer analysis, the tissue is considered to be a homogeneous domain, with a perfusion coefficient and effective scattering coefficient dependent on tissue thermal damage. The blood velocity in the capillaries is assumed to be dependent on perfusion and has an impact on the value of the maximum oxygen supply rate. In the PDT model, equations of concentration for triplet oxygen, singlet oxygen and photosensitizer are taken into account;

additionally, the tumor region is distinguished in the PDT model by the assumption of a specific vascular pattern model. At the stage of numerical realization, the boundary element method and the finite difference method are used.

2. Governing equations

The 2D tissue domain subjected to the laser beam is shown in Fig. 1. In the thermal analysis, the tissue domain is treated as homogeneous, whereas the tumor subdomain, marked with a dotted line, is distinguished in the analysis related to reactions occurring during PDT treatment.

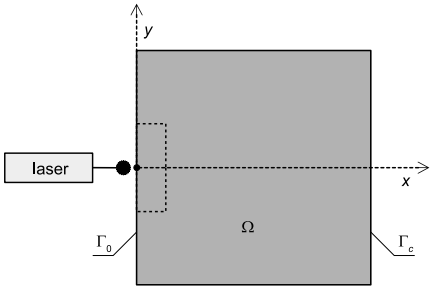

Fig. 1. The domain considered.

The first part of the analysis is related to laser energy deposition. The results obtained in this part will later be used in both the bioheat transfer model and the PDT model.

The total fluence rate ϕ [$\mathrm{W \cdot m^{-2}}$] is the sum of collimated ϕ_c and diffused parts ϕ_d. The collimated part is described using the Beer–Lambert law of absorption [2, 8]:

$$\phi_c(\mathbf{x}) = \phi_0 \exp\left(-\frac{2y^2}{r_{\text{beam}}^2}\right) \exp(-\mu_t' x), \tag{1}$$

while the estimation of diffused part is based on the optical diffusion equation in the form [14, 15, 26, 33, 37]:

$$\begin{aligned} &\mathbf{x} \in \Omega: \quad \nabla\left[D \nabla \phi_d(\mathbf{x})\right] - \mu_a \phi_d(\mathbf{x}) + \mu_s' \phi_c(\mathbf{x}) = 0, \\ &\mathbf{x} \in \Gamma: \quad -\nabla\left[D \phi_d(\mathbf{x})\right] \cdot \mathbf{n} = \frac{1}{2} \phi_d(\mathbf{x}), \\ &\qquad D = \frac{1}{3\left[\mu_a + (1-g)\,\mu_s\right]} = \frac{1}{3\mu_t'}, \\ &\qquad \mu_t' = \mu_a + \mu_s' = (1-g)\mu_s, \end{aligned} \tag{2}$$

where μ_a, μ_s, μ_t [m^{-1}] are the absorption, scattering, and attenuation coefficients, respectively, g is the anisotropy coefficient, D is the diffusion coefficient, and ϕ_0 [$\mathrm{W}\cdot\mathrm{m}^{-2}$] is the surface irradiance of the laser. Additionally, μ_s' and μ_t' denote the effective scattering and effective attenuation coefficients, while r_{beam} is the radius of the laser beam. It should be noted that for most soft tissues, the value of ϕ_d is dominant, so ϕ_c is sometimes neglected, especially in models related to the singlet oxygen generation model. However, in the current work, we have included both components of the total fluence rate because we consider both photochemical and photothermal effects.

The second part of the model is associated with thermal analysis. At this stage, we use the Pennes bioheat transfer equation with appropriate boundary-initial conditions [10, 20, 40, 41]:

$$\begin{aligned}
&\mathbf{x}\in\Omega: && c\dot{T}=\lambda\nabla^2 T+Q_{\mathrm{perf}}+Q_{\mathrm{las}}+Q_{\mathrm{met}},\\
&\mathbf{x}\in\Gamma_0: && q(\mathbf{x},t)=\alpha(T-T_{\mathrm{amb}}),\\
&\mathbf{x}\in\Gamma_c: && q(\mathbf{x},t)=0,\\
&t=0: && T(\mathbf{x},t)=T_{\mathrm{init}},
\end{aligned} \tag{3}$$

where λ [$\mathrm{W}\cdot\mathrm{m}^{-1}\cdot\mathrm{K}^{-1}$] is the thermal conductivity, c [$\mathrm{J}\cdot\mathrm{m}^{-3}\cdot\mathrm{K}^{-1}$] is the volumetric specific heat, T denotes the temperature while $\dot{T}$ its time derivative, q [$\mathrm{W}\cdot\mathrm{m}^{-2}$] is the external heat flux, Q_{perf}, Q_{las}, and Q_{met} [$\mathrm{W}\cdot\mathrm{m}^{-3}$] are heat sources related to perfusion, the impact of the laser on tissue and metabolism, respectively, α [$\mathrm{W}\cdot\mathrm{m}^{-2}\cdot\mathrm{K}^{-1}$] is the coefficient of convective heat transfer, T_{amb} is the surrounding temperature, and T_{init} is the initial tissue temperature. The boundary Γ_0 is the external surface of the tissue subjected to laser irradiation, while Γ_c is the remaining part of the boundary.

The metabolic heat source Q_{met} is assumed to be a constant value, while the definitions of the perfusion and laser heat sources are as follows [2, 8, 35, 40]:

$$\begin{aligned}
Q_{\mathrm{perf}}(\mathbf{x},t)&=c_B w\left[T_B-T(\mathbf{x},t)\right],\\
Q_{\mathrm{las}}(\mathbf{x},t)&=\mu_a\phi(\mathbf{x}),
\end{aligned} \tag{4}$$

where w [s^{-1}] is the perfusion coefficient, c_B [$\mathrm{J}\cdot\mathrm{m}^{-3}\cdot\mathrm{K}^{-1}$] is the volumetric specific heat of the blood and T_b corresponds to the arterial temperature. As is visible by the Q_{las}, the total fluence rate ϕ calculated in the first part of the analysis is taken into account as it can be seen in the definition of Q_{las}.

The third part constitutes the model of the reactions that occur during PDT. As previously mentioned, the entire set of coupled differential reaction equations is simplified to a form consisting of equations for the three main agents in PDT processes: triplet oxygen, singlet oxygen, and a photosensitizer [4–8]:

$$\mathbf{x}\in\Omega:\ \begin{cases} \dfrac{\mathrm{d}c_{^3\mathrm{O}_2}}{\mathrm{d}t}+\gamma c_{\mathrm{S}_0}=\psi_{\mathrm{sup}}, & \gamma \ =\dfrac{\xi\phi c_{^3\mathrm{O}_2}}{c_{^3\mathrm{O}_2}+\beta},\\ \dfrac{\mathrm{d}c_{\mathrm{S}_0}}{\mathrm{d}t}+\gamma\sigma c_{\mathrm{S}_0}\left(c_{\mathrm{S}_0}+\delta\right)=0, & \psi_{\mathrm{sup}} \ =\psi_{\mathrm{sup,max}}\left(1-\dfrac{c_{^3\mathrm{O}_2}}{c_{^3\mathrm{O}_2,\mathrm{init}}}\right),\\ \dfrac{\mathrm{d}c_{^1\mathrm{O}_2}}{\mathrm{d}t}-\gamma c_{\mathrm{S}_0}=0, & \end{cases} \tag{5}$$

$$t=0:\quad c_{^3\mathrm{O}_2}=c_{^3\mathrm{O}_2,\mathrm{init}},\quad c_{\mathrm{S}_0}=c_{\mathrm{S}_0,\mathrm{init}},\quad c_{^1\mathrm{O}_2}=0,$$

where $c_{^3\mathrm{O}_2}$, c_{S_0}, $c_{^1\mathrm{O}_2}$ $[\mathrm{mol}\cdot\mathrm{cm}^{-3}]$ are the concentrations of triplet-state oxygen, sensitizer, and singlet-state oxygen, respectively, the parameters β $[\mathrm{mol}\cdot\mathrm{cm}^{-3}]$, σ $[\mathrm{cm}^3\cdot\mathrm{mol}^{-1}]$, ξ $[\mathrm{cm}^2\cdot\mathrm{mW}^{-1}\cdot\mathrm{s}^{-1}]$ and δ $[\mathrm{mol}\cdot\mathrm{cm}^{-3}]$ are the PDT photochemical parameters defined as the oxygen quenching threshold concentration, specific photobleaching ratio, specific oxygen consumption rate, and the low concentration correction term, respectively, ψ_{sup} $[\mathrm{mol}\cdot\mathrm{cm}^{-3}\cdot\mathrm{s}^{-1}]$ is the oxygen supply rate, and $\psi_{\mathrm{sup,max}}$ $[\mathrm{mol}\cdot\mathrm{cm}^{-3}\cdot\mathrm{s}^{-1}]$ is the maximum oxygen supply rate.

The two parameters, that is, the perfusion coefficient w and the effective scattering coefficient μ_s' are assumed to be thermal-damage-dependent [9, 20, 35]:

$$w=w(\mathrm{Arr})=\begin{cases} \left(1+25\mathrm{Arr}-260\mathrm{Arr}^2\right)w_0, & 0\le\mathrm{Arr}\le 0.1,\\ (1-\mathrm{Arr})\,w_0, & 0.1<\mathrm{Arr}\le 1,\\ 0, & \mathrm{Arr}>1, \end{cases} \tag{6}$$

and

$$\mu_s'(\mathrm{Arr})=\mu_{s\,\mathrm{nat}}'\exp(-\mathrm{Arr})+\mu_{s\,\mathrm{den}}'[1-\exp(-\mathrm{Arr})], \tag{7}$$

where w_0 is the initial perfusion coefficient, and $\mu_{s\,\mathrm{nat}}'$ and $\mu_{s\,\mathrm{den}}'$ are effective scattering coefficients for native and denatured tissue (i.e., thermally damaged). In the function of the perfusion coefficient, the range [0, 0.1] corresponds to the increase in perfusion caused by vasodilation, while the interval (0.1, 1] reflects the decrease in blood flow associated with vasculature damage.

In Eqs. (6) and (7), Arr is the Arrhenius integral, probably the most popular model of thermal damage, in the form [16, 26, 37, 40]:

$$\mathrm{Arr}(\mathbf{x},t^F)=\int_0^{t^F}A\exp\left[-\frac{E}{RT(\mathbf{x},t)}\right]\mathrm{d}t, \tag{8}$$

where A $[\mathrm{s}^{-1}]$ is the pre-exponential factor, E $[\mathrm{J}\cdot\mathrm{mol}^{-1}]$ is the activation energy, R $[\mathrm{J}\cdot\mathrm{mol}^{-1}\cdot\mathrm{K}^{-1}]$ is the universal gas constant and w_0 is the initial perfusion coefficient.

As already mentioned, increases in tissue temperature during PDT are rather small, so it is not expected that the Arr = 1 criterion indicating permanent tissue damage will be met. The Arrhenius scheme is used here only because of the functions (6) and (7), which reflect well the phenomena occurring in the tissue during its heating.

The connection between bioheat transfer and PDT models involves, among other things, a variable perfusion coefficient (6). This implies that the velocity of blood in the capillaries, responsible for the delivery of oxygen to the tissues, must also be variable. The relationship may be written as follows [36, 37]:

$$w = \frac{Q_b}{\pi R_t^2 L_t} = \frac{\pi R_c^2 u_b}{\pi R_t^2 L_t} \quad \rightarrow \quad u_b = w(\mathrm{Arr}) L_t \frac{R_t^2}{R_c^2}, \tag{9}$$

where R_c [μm] is the capillary radius, R_t [μm] is the radius of the tissue cylinder around capillary, L_t [μm] is the capillary length, while Q_b [$\mathrm{cm}^3 \cdot \mathrm{s}^{-1}$] and u_b [$\mathrm{cm} \cdot \mathrm{s}^{-1}$] denote the blood flow rate in the capillary and the blood velocity in the capillary, respectively.

Next, the calculated u_b value is used to determine the maximum oxygen supply rate $\psi_{\mathrm{sup,max}}$, which is a component of the PDT model (see Eq. (5)), based on the relationship [5]:

$$\psi_{\mathrm{sup,max}} = \frac{1200 u_b R_c \left(R_c + \frac{a^2 + M_0^2}{2500 - M_0^2}\right)}{L_t \left(R_t + b\right)^2}, \quad \begin{array}{ll} P_b = 100 \text{ mmHg}: & a = 100, \quad b = 4.2, \\ P_b = 50 \text{ mmHg}: & a = 50, \quad b = -4.2, \end{array} \tag{10}$$

where M_0 [$\mathrm{mol} \cdot \mathrm{cm}^{-3} \cdot \mathrm{s}^{-1}$] is the oxygen consumption rate and P_b [mmHg] is the partial pressure of $^3O_2$ in the blood vessel. The value $P_b = 100$ [mmHg] is typical for healthy tissue, while cancer tissue is often hypoxic, so the coefficient values for $P_b = 50$ [mmHg] refer only to this type of tissue.

As stated previously, the tumor region is distinguished in the PDT model by the assumption of a specific vascular pattern model, as described by the above formulas. Details of how this pattern was assumed in the study are explained in Sec. 4.

In Fig. 2, a flowchart of the data between different parts of the analysis is shown. Trapezoids represent input data and the results that will be presented.

3. Methods of solution

In the numerical realization stage, the first scheme of boundary element method (BEM) and finite difference method (FDM) is employed. The discretization and stencil are presented in Fig. 3.

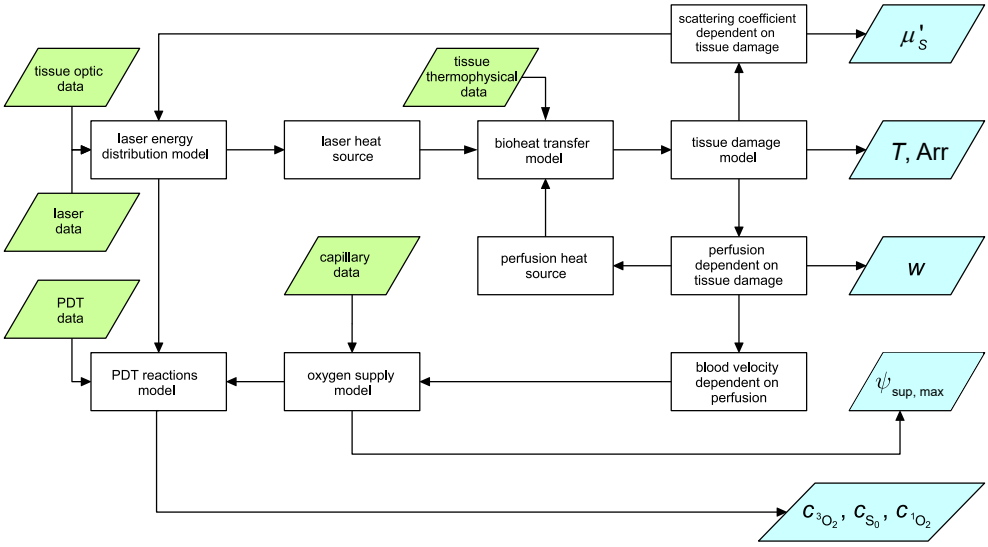

FIG. 2. Data transfer between different parts of the analysis.

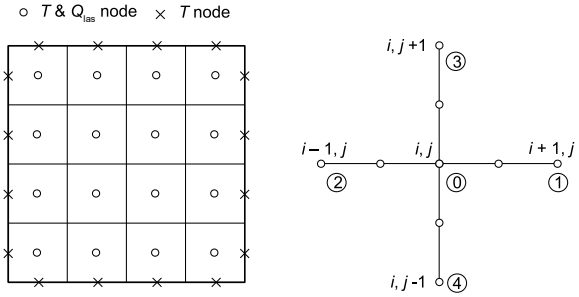

FIG. 3. Discretization used in the bioheat transfer analysis and five-point stencil used in the laser energy deposition task.

For the transient 2D bioheat problem (Eq. (3)), for the time grid with a constant step Δt, the boundary integral equation corresponding to transition $t^{f-1} \to t^f$ takes the form (in this study, constant boundary elements were used) [42, 43]:

$$B(\zeta)T(\mathbf{x},t^f) + \int_\Gamma q(\mathbf{x},t^f)g(\zeta,\mathbf{x})\,\mathrm{d}\Gamma = \int_\Gamma T(\mathbf{x},t^f)h(\zeta,\mathbf{x})\,\mathrm{d}\Gamma + \iint_\Omega q^*(\zeta,\mathbf{x},t^f,t^{f-1})T(\mathbf{x},t^{f-1})\,\mathrm{d}\Omega + \iint_\Omega Q_V(\mathbf{x},t^{f-1})g(\zeta,\mathbf{x})\,\mathrm{d}\Omega, \quad (11)$$

where Q_V denotes the sum of the internal heat function associated with perfusion, metabolism, and laser irradiation (see Eq. (3)), T^* and q^* are the fun-

damental solution and the heat flux resulting from the fundamental solution, respectively, [20]:

$$T^*(\zeta, \mathbf{x}, t^f, t) = \frac{1}{4\pi a(t^f - t)} \exp\left[-\frac{r^2}{4a(t^f - t)}\right], \quad q^* = -\lambda \nabla T^* \mathbf{n}, \tag{12}$$

where r is the distance from the point under consideration $\mathbf{x}$ to the observation point ζ, $a = \lambda/c$, $B(\zeta)$ is the coefficient from the interval (0, 1) and

$$h(\zeta, \mathbf{x}) = \frac{1}{c} \int\limits_{t^{f-1}}^{t^f} q^*(\zeta, \mathbf{x}, t^f, t)\, \mathrm{d}t, \qquad g(\zeta, \mathbf{x}) = \frac{1}{c} \int\limits_{t^{f-1}}^{t^f} T^*(\zeta, \mathbf{x}, t^f, t)\, \mathrm{d}t. \tag{13}$$

The discrete form of Eq. (11) used in numerical realization is as follows (N – the number of boundary elements, L – the number of internal elements) [42]:

$$\sum_{j=1}^{N} G_{ij} q_j^f = \sum_{j=1}^{N} H_{ij} T_j^f + \sum_{l=1}^{L} P_{il} T_l^{f-1} + \sum_{l=1}^{L} Z_{il} Q_{Vl}^{f-1}, \tag{14}$$

where

$$G_{ij} = \int\limits_{\Gamma_j} g(\zeta^i, \mathbf{x})\, \mathrm{d}\Gamma_j, \qquad H_{ij} = \begin{cases} \displaystyle\int\limits_{\Gamma_j} h(\zeta^i, \mathbf{x})\, \mathrm{d}\Gamma_j, & i \neq j, \\ -0.5, & i = j, \end{cases}$$
$$P_{il} = \iint\limits_{\Omega_l} T^*(\zeta^i, \mathbf{x}, t^f, t^{f-1})\, \mathrm{d}\Omega_l, \quad Z_{il} = \iint\limits_{\Omega_l} g(\zeta^i, \mathbf{x})\, \mathrm{d}\Omega_l. \tag{15}$$

After determining the "missing" boundary values of the temperatures and heat fluxes, the values of the temperatures at the internal points ζ^i for time t^f are calculated using the formula ($i = N + 1, ..., N + L$) [42]:

$$T_i^f = \sum_{j=1}^{N} H_{ij} T_j^f - \sum_{j=1}^{N} G_{ij} q_j^f + \sum_{l=1}^{L} P_{il} T_l^{f-1} + \sum_{l=1}^{L} Z_{il} Q_{Vl}^{f-1}. \tag{16}$$

For solving the optical diffusion Eq. (2), the FDM is used. The following differential quotients for the stencil presented in Fig. 3 are used (l is the grid step) [40, 41]:

$$\left(D\frac{\partial \phi_d}{\partial x_1}\right)_{i+0.5,j} = D_{01}\frac{\phi_{d1} - \phi_{d0}}{l}, \qquad \left(D\frac{\partial \phi_d}{\partial x_1}\right)_{i-0.5,j} = D_{02}\frac{\phi_{d0} - \phi_{d2}}{l},$$
$$\left(D\frac{\partial \phi_d}{\partial x_2}\right)_{i,j+0.5} = D_{03}\frac{\phi_{d3} - \phi_{d0}}{l}, \qquad \left(D\frac{\partial \phi_d}{\partial x_2}\right)_{i,j-0.5} = D_{04}\frac{\phi_{d0} - \phi_{d4}}{l}, \tag{17}$$

where

$$D_{0e} = \frac{2D_0 D_e}{D_0 + D_e}. \tag{18}$$

So, the operator on the left-hand side of (2), for the central node, can be written as:

$$\left[\frac{\partial}{\partial x_1}\left(D\frac{\partial \phi_d}{\partial x_1}\right) + \frac{\partial}{\partial x_2}\left(D\frac{\partial \phi_d}{\partial x_2}\right)\right]_{i,j} = \frac{1}{l}\sum_{e=1}^{4} D_{0e}\left(\phi_{de} - \phi_{d0}\right). \tag{19}$$

The final equation for the central node of the stencil can be written in the form:

$$\phi_{d0} = \frac{\sum\limits_{e=1}^{4} D_{0e}\left(\phi_{de} - \phi_{d0}\right) + l\mu_s'\phi_{c0}}{\sum\limits_{e=1}^{4} D_{0e} + l\mu_a}. \tag{20}$$

Also, to solve the PDT model (5), the FDM is used. In this case, the difference quotients are substituted in place of the derivative with respect to time, so finally, the difference equations take the form [40, 41]:

$$\begin{aligned}
c^f_{\mathrm{S}_0,i} &= c^{f-1}_{\mathrm{S}_0,i} - \Delta t \frac{\sigma\xi\phi c^{f-1}_{\mathrm{S}_0,i} c^{f-1}_{^3\mathrm{O}_2,i}\left(c^{f-1}_{\mathrm{S}_0,i} + \delta\right)}{c^{f-1}_{^3\mathrm{O}_2,i} + \beta}, \\
c^f_{^3\mathrm{O}_2,i} &= c^{f-1}_{^3\mathrm{O}_2,i} - \Delta t\left[\frac{\xi\phi c^{f-1}_{\mathrm{S}_0,i} c^{f-1}_{^3\mathrm{O}_2,i}}{c^{f-1}_{^3\mathrm{O}_2,i} + \beta} + \psi_{\mathrm{sup,max}}\left(1 - \frac{c^{f-1}_{^3\mathrm{O}_2,i}}{c_{^3\mathrm{O}_2,\mathrm{init}}}\right)\right], \\
c^f_{^1\mathrm{O}_2,i} &= c^{f-1}_{^1\mathrm{O}_2,i} + \Delta t \frac{\xi\phi c^{f-1}_{\mathrm{S}_0,i} c^{f-1}_{^3\mathrm{O}_2,i}}{c^{f-1}_{^3\mathrm{O}_2,i} + \beta}.
\end{aligned} \tag{21}$$

4. Results of computations

In this research, a square area of tissue with dimensions of 4×4 cm was analyzed. The tissue area was treated as homogeneous for thermal analysis. An area with tumor was also modeled, distinguished only in the PDT part of the analysis. For the BEM analysis, the interior of the domain was discretized by dividing it into 1600 elements, and the boundary into 160 boundary elements. For FDM, the domain was discretized using 40×40 nodes.

To describe the transfer of bioheat and the distribution of light, the following thermophysical and optical parameters of tissues and blood and the

values in the boundary-initial conditions were used: $\lambda = 0.75\ \mathrm{W \cdot m^{-1} \cdot K^{-1}}$, $c = 3\ \mathrm{MJ \cdot m^{-3} \cdot K^{-1}}$, $w_0 = 0.00125\ \mathrm{s^{-1}}$, $\mu_a = 103\ \mathrm{m^{-1}}$, $\mu'_{s\,\mathrm{nat}} = 1346\ \mathrm{m^{-1}}$, $\mu'_{s\,\mathrm{den}} = 2692\ \mathrm{m^{-1}}$, $Q_{\mathrm{met}} = 250\ \mathrm{W \cdot m^{-3}}$, $c_B = 3.9962\ \mathrm{MJ \cdot m^{-3} \cdot K^{-1}}$, $T_B = 37°\mathrm{C}$, $\alpha = 10\ \mathrm{W \cdot m^{-2} \cdot K^{-1}}$, $T_{\mathrm{amb}} = 20°\mathrm{C}$, and $T_{\mathrm{init}} = 37°\mathrm{C}$. Values necessary for the tissue damage model are: $A = 1.98 \cdot 10^{106}\ \mathrm{s^{-1}}$, $E = 6.67 \cdot 10^5\ \mathrm{J \cdot mol^{-1}}$, $R = 8.314\ \mathrm{J \cdot mol^{-1} \cdot K^{-1}}$ [10, 20, 26, 35].

The following photochemical parameters were applied in the PDT model: $\beta = 11.9 \cdot 10^{-9}\ \mathrm{mol \cdot cm^{-3}}$, $\sigma = 7.6 \cdot 10^4\ \mathrm{cm^3 \cdot mol^{-1}}$, $\xi = 3.7 \cdot 10^{-3}\ \mathrm{cm^2 \cdot mW^{-1} \cdot s^{-1}}$, $\delta = 33 \cdot 10^{-9}\ \mathrm{mol \cdot cm^{-3}}$ and initial concentrations $c_{^3\mathrm{O}_2,\mathrm{init}} = 83 \cdot 10^{-9}\ \mathrm{mol \cdot cm^{-3}}$ (for healthy tissue), $c_{^3\mathrm{O}_2,\mathrm{init}} = 39.41 \cdot 10^{-9}\ \mathrm{mol \cdot cm^{-3}}$ (for tumor tissue), and $c_{\mathrm{S}_0,\mathrm{init}} = 7 \cdot 10^{-9}\ \mathrm{mol \cdot cm^{-3}}$. These values correspond to the parameters of the photosensitizer Photofrin at 630 nm [5].

The duration of the PDT procedure varies, but usually ranges from a few to several minutes. A 3600 s laser exposure was used for the analysis [5]. Calculations were carried out for the constant surface irradiance of the laser $\phi_0 = 300\ \mathrm{mW \cdot cm^{-2}}$ and the radius of the laser beam $r_{\mathrm{beam}} = 1$ mm.

It should be noted that analysis related to bioheat and PDT requires different time steps. The time step for bioheat is 1 s, while the time step for PDT is 0.1 s. Due to this, the bioheat results, which are necessary for the PDT model, are linearly interpolated, and then we obtain the necessary values.

As mentioned earlier, cancerous tissue is different from healthy tissue. In the current work, we take into account differences between tissues resulting from abnormal vascular pattern during PDT-related analysis. In healthy tissue, it is assumed, according to the Krogh model, that blood vessels are arranged regularly and parallel to each other, in such a way that each capillary supplies oxygen to the surrounding cylindrical area of tissue. In tumor tissue, capillaries are irregularly distributed and also have irregular shapes, leading to uneven oxygen distribution, often with areas of hypoxia. We incorporated these tumor and the Krogh model features in two ways (Fig. 4).

First, we assumed five types of capillaries, designated as C1–C5 (Table 1). The C1 capillary was assumed to be typical of an area of healthy tissue. Next, the distribution of capillaries in the tumor tissue subdomain was randomly distributed (Fig. 4b), using the discretization assumed in the bioheat transfer task solved by BEM (i.e., capillary types were assigned to the corresponding internal elements of BEM discretization). The second characteristic of the tumor region is the random distribution of the oxygen consumption rate, with values in the range of $M_0 = 0.9 \cdot 10^{-9} \div 6 \cdot 10^{-9}\ \mathrm{mol \cdot cm^{-3} \cdot s^{-1}}$, and assuming a constant value of $M_0 = 2.4 \cdot 10^{-9}\ \mathrm{mol \cdot cm^{-3} \cdot s^{-1}}$ for the area of healthy tissue (Fig. 4c) [5].

The results of time-varying parameter calculations are presented for selected capillaries lying near the external boundary Γ_0 of the tissue, close to the main optical axis of the laser beam (Fig. 4a).

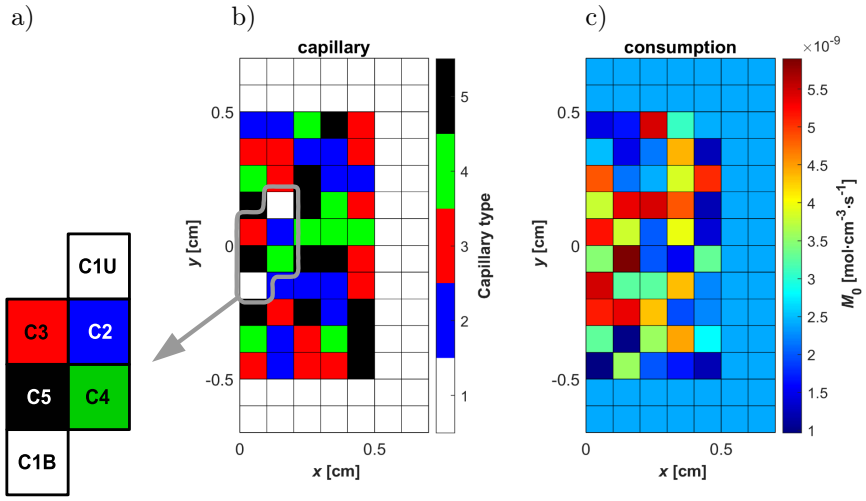

FIG. 4. The model of the abnormal vascular pattern in tumor tissue: a) selected capillaries, b) random distribution of capillaries, and c) random distribution of oxygen consumption rate.

TABLE 1. The capillaries used in the model of an abnormal vascular pattern.

Capillary type	R_c [µm]	R_t [µm]	L_t [µm]
C1	2.5	30	400
C2	10	60	100
C3	4	60	220
C4	10	30	220
C5	4	30	100

Figures 5 and 6 show the histories of parameters associated with the bioheat transfer analysis. As can be seen, the temperature for most capillaries is below

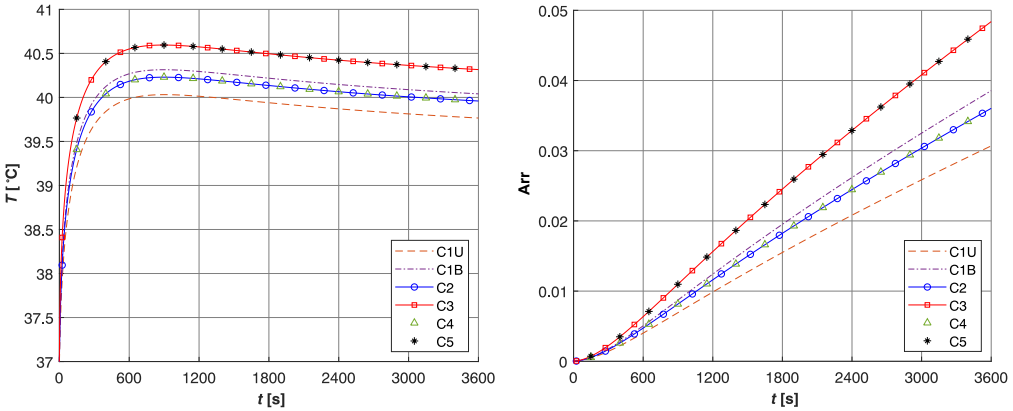

FIG. 5. History of temperature and Arrhenius integral.

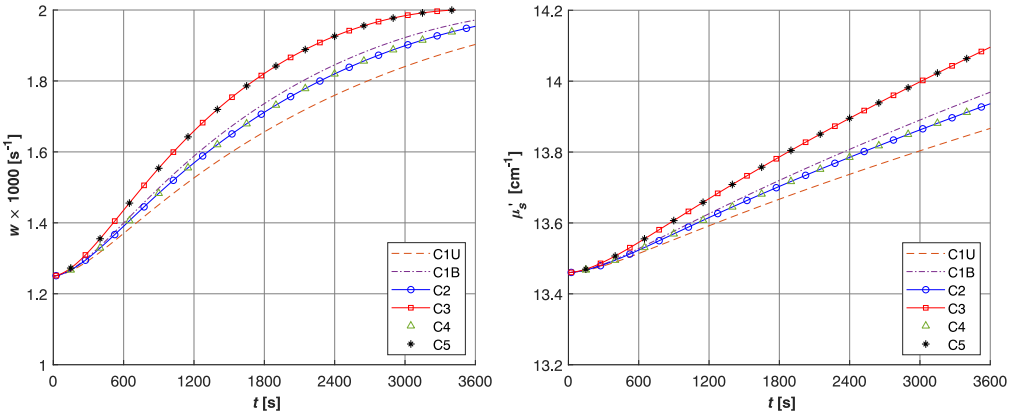

FIG. 6. History of perfusion coefficient and effective scattering coefficient.

40.5°C; only for C3 and C5 it exceeds this value. The value of the Arrhenius integral, although increasing throughout the simulation, is below the 0.05 value. The perfusion function, which was used in the work, indicates that the vasculature is in the stage of vasodilation during the whole simulation (see Eq. (6)). In addition, the value of the effective scattering coefficient increases throughout the simulation according to the function (7).

Figure 7 shows the history of the oxygen maximum supply rate $\psi_{\text{sup,max}}$ calculated from the formula (10). Among other things, capillary parameters were used to determine this value to account for irregularities in the tumor area and the variable value of blood velocity in the capillaries resulting from (9). The value of the maximum supply rate affects the other parameters determined in the PDT model, i.e., the concentrations of triplet oxygen (Fig. 7), photosensi-

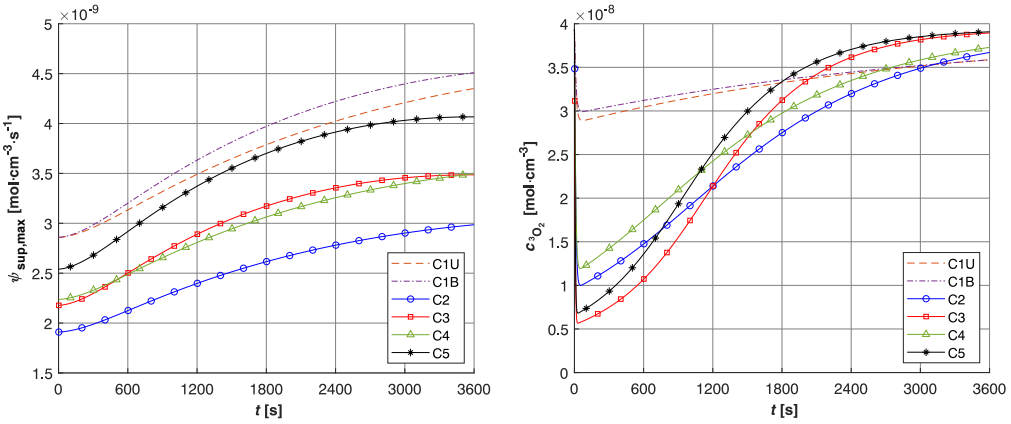

FIG. 7. Histories of oxygen maximum supply rate and $^3O_2$ concentration.

tizer (Fig. 8 left) and single oxygen (Fig. 8 right). A particular characteristic is the sharp drop in triplet oxygen concentration at the beginning of the process, coinciding with the highest photosensitizer concentration.

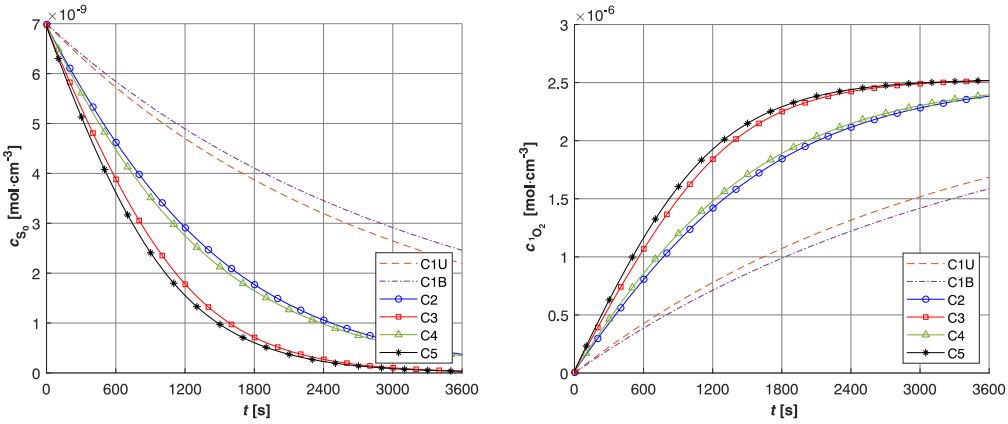

FIG. 8. Histories of S_0 and $^1O_2$ concentrations.

Also, Figs. 9–12 refer to the PDT model. They show the distributions of each parameter at times of 1200, 2400 and 3600 s. In the case of the oxygen supply rate, irregularities in the subdomain of the tumor tissue are clearly visible. For the $^3O_2$ concentration, changes occur only in the tumor region, while in the healthy tissue subdomain, the concentration value is kept constant throughout treatment. For photosensitizer concentration and singlet oxygen, irregularities in the distributions are less pronounced because of the association of these parameters with laser energy deposition in tissue. In addition, for the concentration of photosensitizer, a steady decrease in its concentration throughout the tissue is visible.

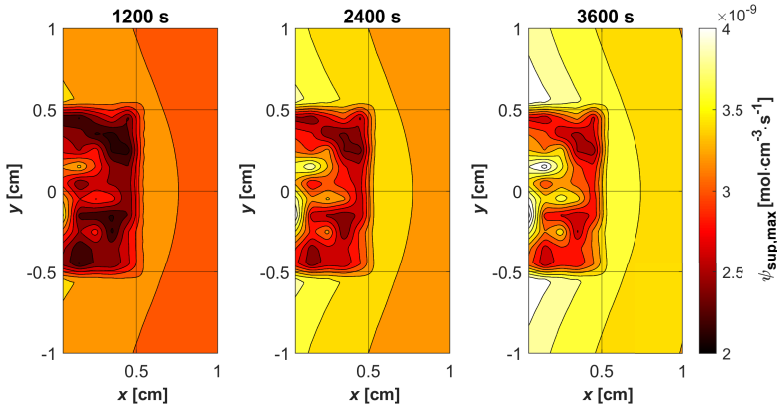

FIG. 9. Distributions of maximum oxygen supply rate.

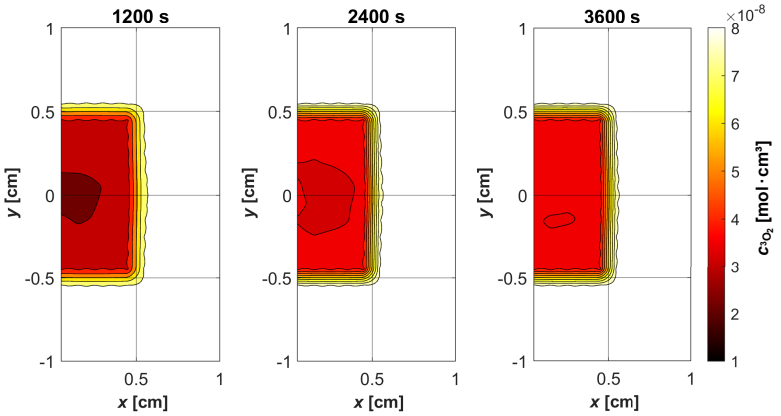

FIG. 10. Distributions of $^3O_2$ concentration.

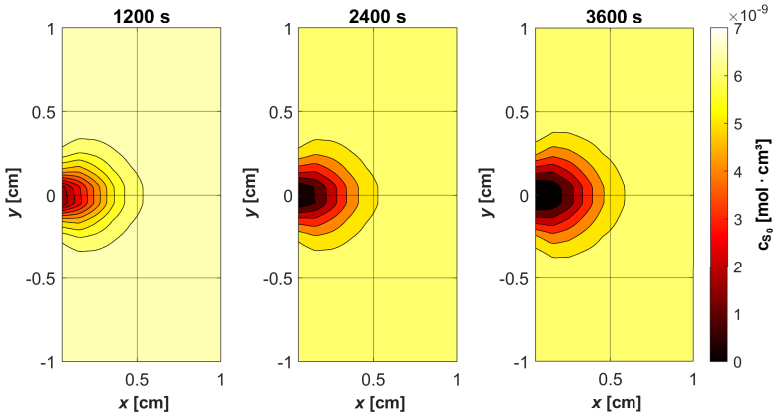

FIG. 11. Distributions of S_0 concentration.

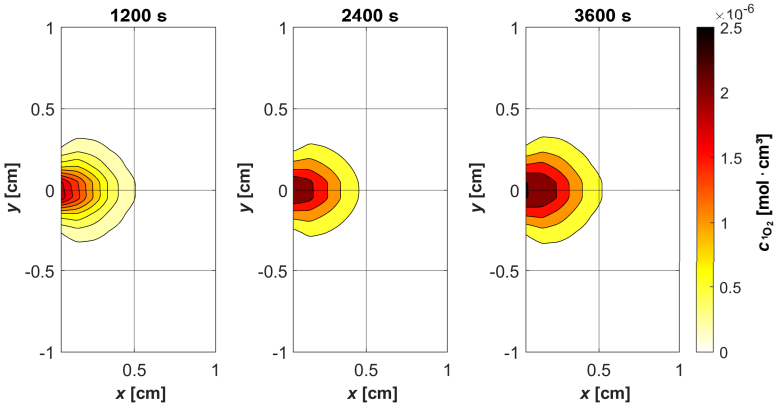

FIG. 12. Distributions of $^1O_2$ concentration.

In this study, the relationship (10) not only accounts for heterogeneities due to the distribution of capillaries in the tumor subdomain but also considers the effect of temperature through the variable value of blood velocity in the capillary u_b (9). Since, so far, bioheat transfer and PDT models have generally been considered separately, without taking into account such effects, the velocity u_b has most often been assumed as a constant value. We made comparisons between the results of the model presented in this work (taking into account the effect of temperature on the PDT process) and PDT simulations that assumed a constant u_b value in the relationship (10) (corresponding to the absence of a link between the bioheat transfer model and the PDT). Furthermore, it was assumed that in all simulations related to comparisons, the oxygen consumption rate $M_0 = 2.4 \cdot 10^{-9}$ mol $\cdot$ cm$^{-3} \cdot$ s^{-1} was for the entire tissue domain, which is the same as for healthy tissue presented earlier. The adopted velocity constants $u_b = 0.005, 0.01, 0.015, 0.02$ cm $\cdot$ s^{-1} correspond to the values found in the literature [5].

Table 2 shows the oxygen maximum supply rate $\psi_{\text{sup,max}}$ values obtained from (10). In calculations that take into account the effect of perfusion on u_b, the value increased throughout the simulation, so the minimum and maximum values correspond to the beginning and end of the simulation ($t = 0$ and 3600 s, respectively). As can be seen, the values obtained for the variable u_b have a similar order of magnitude to each other, while the values obtained for the constant temperature value vary over a fairly large range. For capillaries C2, C4, and C5, the values for variable u_b are lower and outside the range obtained for constant velocity. This is because the u_b values calculated from (9) are lower than the assumed constant u_b values, which in turn is due to the assumed value of the initial perfusion coefficient.

Table 2. Comparison of the maximum oxygen supply rate for variable and constant blood velocity in the capillary.

Capillary	Variable u_b		Constant u_b [cm $\cdot$ s^{-1}]			
	$t = 0$	$t = 3600$ s	0.005	0.01	0.015	0.02
C1U	$2.84 \cdot 10^{-9}$	$4.33 \cdot 10^{-9}$	$1.97 \cdot 10^{-9}$	$3.95 \cdot 10^{-9}$	$5.92 \cdot 10^{-9}$	$7.90 \cdot 10^{-9}$
C1B	$2.84 \cdot 10^{-9}$	$4.49 \cdot 10^{-9}$	$1.97 \cdot 10^{-9}$	$3.95 \cdot 10^{-9}$	$5.92 \cdot 10^{-9}$	$7.90 \cdot 10^{-9}$
C2	$1.91 \cdot 10^{-9}$	$2.98 \cdot 10^{-9}$	$2.12 \cdot 10^{-8}$	$4.24 \cdot 10^{-8}$	$6.36 \cdot 10^{-8}$	$8.48 \cdot 10^{-8}$
C3	$2.17 \cdot 10^{-9}$	$3.47 \cdot 10^{-9}$	$1.75 \cdot 10^{-9}$	$3.51 \cdot 10^{-9}$	$5.26 \cdot 10^{-9}$	$7.01 \cdot 10^{-9}$
C4	$2.23 \cdot 10^{-9}$	$3.49 \cdot 10^{-9}$	$4.51 \cdot 10^{-8}$	$9.02 \cdot 10^{-8}$	$1.35 \cdot 10^{-7}$	$1.80 \cdot 10^{-7}$
C5	$2.54 \cdot 10^{-9}$	$4.06 \cdot 10^{-9}$	$1.80 \cdot 10^{-8}$	$3.61 \cdot 10^{-8}$	$5.41 \cdot 10^{-8}$	$7.22 \cdot 10^{-8}$

Figure 13 shows the history of the $^3O_2$ concentration, which is most affected by the maximum supply rate. This was done for capillaries C3 and C5 that were close to the Γ_0 boundary.

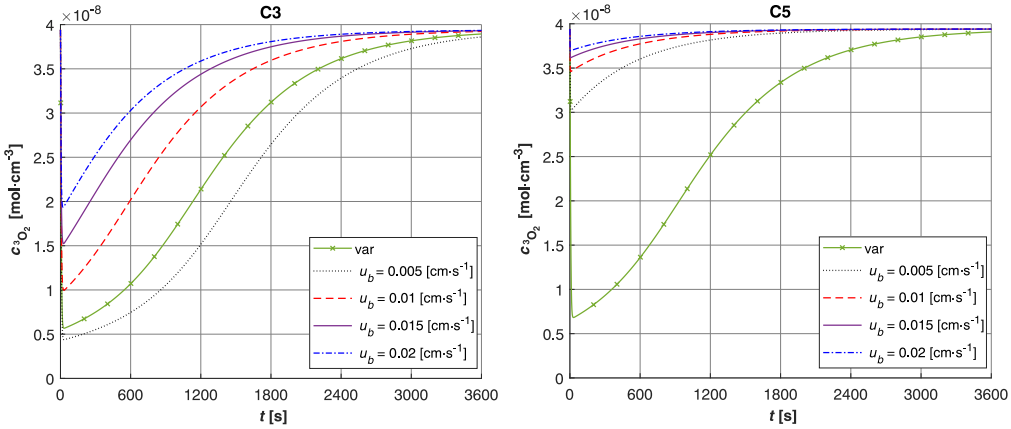

FIG. 13. Comparison of $^3O_2$ concentration for calculations with variable and constant values of blood velocity in the capillary.

5. Discussion and conclusion

In this paper, calculations were performed for the combined bioheat transfer and PDT models. In the PDT model, it was assumed that the capillaries' parameters in the tumor tissue subdomain vary, which captures some of the characteristics of this type of tissue associated with an abnormal vascular pattern. As the results of the calculations show for the assumed laser impulse parameters, there is a temperature increase that does not cause thermal damage to the tissue but changes the values of the perfusion coefficient and effective scattering coefficient (Figs. 5 and 6). The increase in temperature has an apparent effect on the increase in perfusion and consequently on capillary blood velocity. The latter parameter, the capillary dimensions (R_c, R_t, L_t), and the value of the oxygen consumption rate also affect the distribution of the maximum oxygen supply rate (Figs. 7 and 9). Reactions associated with the transition from triplet to singlet oxygen occur most rapidly at the beginning of therapy, with a concentration of photosensitizer close to the initial one.

Comparisons were also conducted for calculations with constant and variable blood velocity in capillaries, the latter option corresponding to the connection between bioheat transfer and PDT models. Values obtained for the maximum oxygen supply rate for constant u_b values in some capillaries (C2, C4 and C5) (Table 2) are slightly different from the range of values obtained during simulations with a variable u_b related to the perfusion coefficient. This is primarily due to the assumed value of the initial perfusion coefficient ($w_0 = 0.00125$ s^{-1}), one of several common values often used in various bioheat transfer tasks. It is obvious that adopting a value for this coefficient more closely related to the type of soft tissue under consideration would bring their ranges closer together. Ulti-

mately, these results affect the course of the reaction during PDT, particularly the concentration of $^3O_2$.

In the study, a laser beam was adopted as the light source, causing irregularities in the tumor subdomain primarily visible in the maximum supply rate and triplet oxygen concentration. However, different types of light sources, such as linear ones, were used during PDT treatments, which undoubtedly had an impact on the parameter distributions of the PDT model [1, 44].

To the best of our knowledge, the combined bioheat transfer and PDT models have not been considered to date. Previous works generally assumed a constant oxygen maximum supply rate or its value calculated on the basis of an appropriate relationship (see Eq. (10)) with the assumption of constant blood velocity in the capillary. Constant light energy deposition was also usually assumed. However, in our previous work [8], we showed that, assuming the constancy of the aforementioned parameters, our model agrees with the results reported in the literature [44].

As outlined in the paper, although PDT treatments rely primarily on reactions resulting from the presence of oxygen and photosensitizer in the tissue, considering these phenomena in conjunction with the bioheat transfer model makes sense, as temperature can ultimately be a factor in the presence of oxygen in the treated area. In addition, through appropriate parameter functions, it can influence tissue parameters (see Eqs. (21) and (7)). It should also be noted that the proposed combination of models does not take into account all the phenomena that affect the presence of oxygen in the tissue. Among other things, it depends on the degree of saturation of oxyhemoglobin, which is related to the partial pressure in the blood. The relationship between these two parameters is expressed by the dissociation curve of oxyhemoglobin, which changes its shape under the influence of temperature (the so-called Bohr effect) [12, 19, 36–38]. To include this phenomenon in the model, one would need to consider an additional microscale model based on the Krogh cylinder, instead of the simplified formula used in the current work (see Eq. (10)).

Various photosensitizers characterized by different values of the photochemical parameters (ξ, δ, β, and σ) are used during PDT therapy. A good method to account for potential differences in the course of therapy may be sensitivity analysis. It also allows to consider variations in tissue parameters due to individual characteristics [23, 45].

The bioheat transfer model used is the Pennes equation. This equation, of course, has many disadvantages compared to the latest dual-phase-lag model equations, based on the theory of porous bodies, allowing, among other things, to take into account delays in the propagation of temperature and heat flux in the tissue. One of the basic parameters of this equation is porosity, which is related to the density distribution of blood vessels in the tissue area [27–29, 31, 34].

Considering the method for modeling tumor tissue proposed in the paper, the use of the DPL equation in conjunction with the PDT model seems interesting. This will certainly be one of the directions of development for the proposed model.

The conclusion of the model presented using the combined bioheat and PDT models is that even in treatments where there is no distinct heating of the tissue, temperature should be taken into account as one of the potential factors that can influence the course of treatment through various processes. This appears to be particularly relevant in cancer and experimental immunology, where it has been shown to affect the regulation of the immune response and the dynamics of the tumor microenvironment.

Acknowledgements

The research was funded from the projects of the Silesian University of Technology, Faculty of Mechanical Engineering.

References

1. M.H. Abdel-Kader, *Photodynamic Therapy: From Theory to Application*, Springer-Verlag, Berlin, Heidelberg, 2016.
2. M.H. Niemz, *Laser-Tissue Interactions: Fundamentals and Applications*, Springer-Verlag, Berlin, Heidelberg, 2007.
3. J.F. Algorri, M. Ochoa, P. Roldán-Varona, L. Rodríguez-Cobo, J.M. López-Higuera, Light technology for efficient and effective photodynamic therapy: A critical review, *Cancers*, **13**(14): 3484, 2021, doi: 10.3390/cancers13143484.
4. T.C. Zhu, M.M. Kim, X. Liang, J.C. Finlay, T.M. Busch, In-vivo singlet oxygen threshold doses for PDT, *Photonics and Lasers in Medicine*, **4**(1): 59–71, 2015, doi: 10.1515/PLM-2014-0037.
5. T.C. Zhu, B. Liu, R. Penjweini, Study of tissue oxygen supply rate in a macroscopic photodynamic therapy singlet oxygen model, *Journal of Biomedical Optics*, **20**(3): 038001, 2015, doi: 10.1117/1.jbo.20.3.038001.
6. M.M. Kim, A. Darafsheh, Light sources and dosimetry techniques for photodynamic therapy, *Photochemistry and Photobiology*, **96**(2): 280–294, 2020, doi: 10.1111/php.13219.
7. T. Sheng, Y. Ong, W. Guo, T.C. Zhu, Reactive oxygen species explicit dosimetry to predict tumor growth for benzoporphyrin derivative-mediated vascular photodynamic therapy, *Journal of Biomedical Optics*, **25**(6): 063805, 2020, doi: 10.1117/1.jbo.25.6.063805.
8. M. Jasiński, M. Zadoń, Mathematical modeling of the phenomena that occur in a biological tissue containing a photosensitizer, *Journal of Applied Mathematics and Computational Mechanics*, **21**(4): 40–51, 2022, doi: 10.17512/jamcm.2022.4.04.
9. J.P. Abraham, E.M. Sparrow, A thermal-ablation bioheat model including liquid-to-vapor phase change, pressure- and necrosis-dependent perfusion, and moisture-dependent prop-

erties, *International Journal of Heat and Mass Transfer*, **50**(13–14): 2537–2544, 2007, doi: 10.1016/j.ijheatmasstransfer.2006.11.045.

10. M. Paruch, Mathematical modeling of breast tumor destruction using fast heating during radiofrequency ablation, *Materials*, **13**(1): 136, 2020, doi: 10.3390/MA13010136.

11. T.W. Secomb, J.P. Alberding, R. Hsu, M.W. Dewhirst, A.R. Pries, Angiogenesis: An adaptive dynamic biological patterning problem, *PLoS Computational Biology*, **9**(3): e1002983, 2013, doi: 10.1371/journal.pcbi.1002983.

12. D. Goldman, Theoretical models of microvascular oxygen transport to tissue, *Microcirculation*, **15**(8): 795–811, 2008, doi: 10.1080/10739680801938289.

13. L.A. Dombrovsky, D. Baillis, *Thermal Radiation in Disperse Systems: An Engineering Approach*, Begell House, New York, 2010.

14. S.L. Jacques, B.W. Pogue, Tutorial on diffuse light transport, *Journal of Biomedical Optics*, **13**(4): 041302, 2008, doi: 10.1117/1.2967535.

15. L.A. Dombrovsky, The use of transport approximation and diffusion-based models in radiative transfer calculations, *Computational Thermal Sciences*, **4**(4): 297–315, 2012, doi: 10.1615/ComputThermalScien.2012005050.

16. L.A. Dombrovsky, J.H. Randrianalisoa, W. Lipinski, V. Timchenko, Simplified approaches to radiative transfer simulations in laser-induced hyperthermia of superficial tumors, *Computational Thermal Sciences*, **5**(6): 521–530, 2013, doi: 10.1615/Comput ThermalScien.2013008157.

17. M. Friebel, A. Roggan, G.J. Müller, M.C. Meinke, Determination of optical properties of human blood in the spectral range 250 to 1100 nm using Monte Carlo simulations with hematocrit-dependent effective scattering phase functions, *Journal of Biomedical Optics*, **11**(3): 034021, 2006, doi: 10.1117/1.2203659.

18. A. Paul, A. Paul, Computational study of photo-thermal ablation of large blood vessel embedded tumor using localized injection of gold nanoshells, *Journal of Thermal Biology*, **78**: 329–342, 2018, doi: 10.1016/j.jtherbio.2018.10.021.

19. Y. He, M. Shirazaki, H. Liu, R. Himeno, Z. Sun, A numerical coupling model to analyze the blood flow, temperature, and oxygen transport in human breast tumor under laser irradiation, *Computers in Biology and Medicine*, **36**(12): 1336–1350, 2006, doi: 10.1016/j.compbiomed.2005.08.004.

20. M. Jasiński, Numerical analysis of thermal damage and oxygen distribution in laser irradiated tissue, *Journal of Applied Mathematics and Computational Mechanics*, **21**(2): 51–62, 2022, doi: 10.17512/jamcm.2022.2.05.

21. R.A. El-Nabulsi, Fractal Pennes and Cattaneo–Vernotte bioheat equations from product-like fractal geometry and their implications on cells in the presence of tumour growth, *Journal of the Royal Society Interface*, **18**(182): 20210564, 2021, doi: 10.1098/RSIF.2021.0564.

22. R.A. El-Nabulsi, W. Anukool, Nonlocal thermal effects on biological tissues and tumors, *Thermal Science and Engineering Progress*, **34**: 101424, 2022, doi: 10.1016/j.tsep.2022.101424.

23. B. Mochnacki, M. Ciesielski, Sensitivity of transient temperature field in domain of forearm insulated by protective clothing with respect to perturbations of external boundary

heat flux, *Bulletin of the Polish Academy of Sciences: Technical Sciences*, **64**(3): 591–598, 2016, doi: 10.1515/bpasts-2016-0066.

24. S.C. Akula, R. Maniyeri, Numerical simulation of bioheat transfer: a comparative study on hyperbolic and parabolic heat conduction, *Journal of the Brazilian Society of Mechanical Sciences and Engineering*, **42**(62): 1–13, 2020, doi: 10.1007/s40430-019-2132-x.

25. S. Hassanpour, A. Saboonchi, Modeling of heat transfer in a vascular tissue-like medium during an interstitial hyperthermia process, *Journal of Thermal Biology*, **62**: 150–158, 2016, doi: 10.1016/j.jtherbio.2016.06.022.

26. E. Majchrzak, L. Turchan, M. Jasiński, Identification of laser intensity assuring the destruction of target region of biological tissue using the gradient method and generalized dual-phase lag equation, *Iranian Journal of Science and Technology – Transactions of Mechanical Engineering*, **43**: 539–548, 2019, doi: 10.1007/s40997-018-0225-2.

27. T. Saeed, I. Abbas, Finite element analyses of nonlinear DPL bioheat model in spherical tissues using experimental data, *Mechanics Based Design of Structures and Machines*, **50**(4): 1287–1297, 2022, doi: 10.1080/15397734.2020.1749068.

28. F. Alzahrani, I. Abbas, A numerical solution of nonlinear DPL bioheat model in biological tissue due to laser irradiations, *Indian Journal of Physics*, **96**(2): 377–383, 2022, doi: 10.1007/s12648-020-01988-w.

29. R.K. Chaudhary, D. Kumar, K.N. Rai, J. Singh, Analysis of thermal injuries using classical Fourier and DPL models for multi-layer of skin under different boundary conditions, *International Journal of Biomathematics*, **14**(6): 2150040, 2021, doi: 10.1142/S1793524521500406.

30. R.K. Chaudhary, D. Kumar, K.N. Rai, J. Singh, Numerical simulation of the skin tissue subjected to hyperthermia treatment using a nonlinear DPL model, *Thermal Science and Engineering Progress*, **34**: 101394, 2022, doi: 10.1016/J.tsep.2022.101394.

31. E. Majchrzak, Ł. Turchan, J. Dziatkiewicz, Modeling of skin tissue heating using the generalized dual phase-lag equation, *Archives of Mechanics*, **67**(6): 417–437, 2015, doi: 10.24423/aom.1777.

32. E. Majchrzak, G. Kałuża, Sensitivity analysis of temperature in heated soft tissues with respect to time delays, *Continuum Mechanics and Thermodynamics*, **34**(2): 587–599, 2021, doi: 10.1007/s00161-021-01075-3.

33. N. Afrin, J. Zhou, Y. Zhang, D.Y. Tzou, J.K. Chen, Numerical simulation of thermal damage to living biological tissues induced by laser irradiation based on a generalized dual phase lag model, *Numerical Heat Transfer Applications, Part A: Applications*, **61**(7): 483–501, 2012, doi: 10.1080/10407782.2012.667648.

34. E. Majchrzak, M. Stryczyński, Dual-phase lag model of heat transfer between blood vessel and biological tissue, *Mathematical Biosciences and Engineering: MBE*, **18**(2): 1573–1589, 2021, doi: 10.3934/MBE.2021081.

35. T.N. Glenn, S. Rastegar, S.L. Jacques, Finite element analysis of temperature controlled coagulation in laser irradiated tissue, *IEEE Transactions on Biomedical Engineering*, **43**(1): 79–87, 1996, doi: 10.1109/10.477703.

36. B.J. McGuire, T.W. Secomb, A theoretical model for oxygen transport in skeletal muscle under conditions of high oxygen demand, *Journal of Applied Physiology*, **91**(5): 2255–2265, 2001, doi: 10.1152/jappl.2001.91.5.2255.

37. M. Jasiński, Numerical analysis of the temperature impact to the oxygen distribution in the biological tissue, *Journal of Applied Mathematics and Computational Mechanics*, **19**(3): 17–28, 2020, doi: 10.17512/jamcm.2020.3.02.

38. J.P. Whiteley, D.J. Gavaghan, C.E.W. Hahn, Mathematical modelling of oxygen transport to tissue, *Journal of Mathematical Biology*, **44**(6): 503–522, 2002, doi: 10.1007/s002850200135.

39. B.C. Fry, T.K. Roy, T.W. Secomb, Capillary recruitment in a theoretical model for blood flow regulation in heterogeneous microvessel networks, *Physiological Reports*, **1**(3): e00050, 2013, doi: 10.1002/phy2.50.

40. A. Korczak, M. Jasiński, Modelling of biological tissue damage process with application of interval arithmetic, *Journal of Theoretical and Applied Mechanics*, **57**(1): 249–261, 2019, doi: 10.15632/jtam-pl.57.1.249.

41. B. Mochnacki, A. Piasecka Belkhayat, Numerical modeling of skin tissue heating using the interval finite difference method, *Molecular & Cellular Biomechanics*, **10**(3): 233–244, 2013, doi: 10.3970/mcb.2013.010.233.

42. C.A. Brebbia, J. Domínguez, *Boundary Elements: An Introductory Course*, 2nd ed., WIT Press, London, 1992.

43. E. Majchrzak, Ł. Turchan, The general boundary element method for 3D dual-phase lag model of bioheat transfer, *Engineering Analysis with Boundary Elements*, **50**: 76–82, 2015, doi: 10.1016/j.enganabound.2014.07.012.

44. K.K.H. Wang, J.C. Finlay, T.M. Busch, S.M. Hahn, T.C. Zhu, Explicit dosimetry for photodynamic therapy: Macroscopic singlet oxygen modeling, *Journal of Biophotonics*, **3**(5–6): 304–318, 2010, doi: 10.1002/jbio.200900101.

45. E. Majchrzak, M. Jasiński, Ł. Turchan, Modeling of laser-soft tissue interactions using the dual-phase lag equation: Sensitivity analysis with respect to selected tissue parameters, *Defect and Diffusion Forum*, **379**: 108–123, 2017, doi: 10.4028/www.scientific.net/ddf.379.108.

Received December 13, 2022; accepted June 3, 2023;
published online December 6, 2023.